Progress in Earth and
Planetary Science

RESEARCH ARTICLE   **Open Access**

Melting relations in the Fe–S–Si system at high pressure and temperature: implications for the planetary core

Takanori Sakairi[1], Eiji Ohtani[1,2*] , Seiji Kamada[1,3], Takeshi Sakai[4], Tatsuya Sakamaki[1] and Naohisa Hirao[5]

Abstract

The phase and melting relations in the Fe–S–Si system were determined up to 60 GPa by using a double-sided laser-heated diamond anvil cell combined with X-ray diffraction. On the basis of the X-ray diffraction patterns, we confirmed that hcp/fcc Fe–Si alloys and Fe_3S are stable phases under subsolidus conditions in the Fe–S–Si system. Both solidus and liquidus temperatures are significantly lower than the melting temperature of pure Fe and both increase with pressure. The slopes of the Fe–S–Si liquidus and solidus curves determined here are smaller than the adiabatic temperature gradients of the liquid cores of Mercury and Mars. Thus, crystallization of their cores started at the core–mantle boundary region.

Keywords: Planetary core, Melting relations, Fe–S–Si system, Diamond anvil cell

Introduction

The Earth's core is mainly composed of an iron alloy, with light elements also required in the core to account for the core density deficit (Birch 1964). Sulfur (S), silicon (Si), oxygen (O), carbon (C), and hydrogen (H) have been identified as the likely light elements (e.g., Poirier 1994; Terasaki 2015). Alloying with light elements significantly affects the physical properties of iron and depresses its melting temperature (e.g., Boehler 1996; Lin et al. 2002; Fischer et al. 2013). There are significant implications for the chemical composition and thermal structure of the Earth's core as a corollary. The melting temperature of an iron alloy is important information for estimating the temperature at the inner–outer core boundary (ICB) of the terrestrial planets. An investigation of the high-pressure phases of iron alloys also helps us to understand the structure of the solid inner core. Among the candidate light elements in the core, sulfur and silicon are considered as major light element components based on geochemical models (e.g., Allégre et al. 1995; Javoy 1995; McDonough 2014) and

high-pressure partitioning experiments (e.g., Hillgren et al. 2000; Sakai et al. 2006). Additionally, some geochemical studies and high-pressure experiments have predicted that sulfur and silicon could be present not only in the core of the Earth but also in the cores of other terrestrial planets such as Mars and Mercury (e.g., Bertka and Fei 1998; Malavergne et al. 2010).

Previous high-pressure studies revealed that sulfur and silicon have different effects on the properties of iron alloys. In the Fe–FeS system, Fe_3S_2, Fe_2S, and Fe_3S have been reported as intermediate phases (e.g., Fei et al. 1997, 2000; Li et al. 2001), and hcp-Fe and Fe_3S are stable as the subsolidus phases up to the core conditions. The eutectic temperature in the Fe–Fe_3S system was measured up to 180 GPa using a diamond anvil cell (DAC) (e.g., Kamada et al. 2010, 2012; Morard et al. 2008). It was revealed that the melting temperature of iron is significantly depressed by the effect of sulfur, and the hcp-Fe phase coexists with partial melts between the solidus and liquidus temperatures. The amount of sulfur in the solid iron increases with increasing pressure at the eutectic temperature (e.g., Kamada et al. 2010, 2012; Li et al. 2001). Fe_3S is the only stable phase up to 250 GPa (Ozawa et al. GRL 2013).

Silicon has a high solubility into iron and forms a solid solution with iron at high pressure (e.g., Kuwayama and

* Correspondence: ohtani@m.tohoku.ac.jp
[1]Department of Earth and Planetary Materials Science, Graduate School of Science, Tohoku University, Sendai 980-8578, Japan
[2]V.S. Sobolev Institute of Geology and Mineralogy, Siberian Branch, Russian Academy of Sciences, Koptyuga Ave. 3, Novosibirsk 630090, Russia
Full list of author information is available at the end of the article

Sakairi *et al. Progress in Earth and Planetary Science* (2017) 4:10

Page 2 of 11

Hirose 2004). The solubility of silicon into solid iron increases with increasing pressure and temperature. The high-pressure phase relations of the Fe–Si alloy have been studied by using a DAC, and it was found that the subsolidus phases of the Fe–Si alloy are related to the amount of silicon in the iron alloy (e.g., Asanuma et al. 2008; Fischer et al. 2013; Lin et al. 2002). There is a stability field of hcp + fcc phases in the alloy with Fe-3.4 wt% Si, whereas the B2 phase coexists with these phases for the alloy with Fe8.85 wt% Si (Fischer et al. 2013). The hcp phase Fe-9 wt% Si is stable to pressure and temperature conditions of the inner core (Tateno et al. 2015). The melting temperature of Fe–Si alloy was determined up to above 100 GPa by laser-heated DAC (LHDAC) experiments, and it was revealed that the effect of silicon on the melting temperature of iron alloy is smaller than that of sulfur (Asanuma et al. 2010; Fischer et al. 2013).

In spite of the importance of the effect of both sulfur and silicon on the physical properties of iron alloy, there are few studies about the melting relations of the Fe–S–Si ternary system. Although some previous studies on the closure of the Fe–S–Si liquid immiscibility gap have been reported by Sanloup and Fei (2004) and Morard and Katsura (2010), their experiments were carried out by using a multianvil apparatus at pressures below 25 GPa, and the details of higher pressure phase relations and melting temperatures in the system were not revealed. We have investigated the phase and melting relations in the Fe–S–Si system up to 60 GPa by using the LHDAC combined with an X-ray diffraction technique. Our results provide important clues for understanding the properties of the cores of Earth, Mars, and Mercury.

Method/Experimental

High pressure was generated by a symmetric-type DAC. The culet sizes of the diamond anvils were 300, 250, or 100 μm, depending on the desired experimental pressures. The starting material was composed of a powder mixture of Fe (99.9%; Wako Pure Chemical Industries, Ltd.), FeS (99.9% purity; Rare Metallic Co., Ltd.), and FeSi (99.9% purity; Rare Metallic Co., Ltd.), which was ground in an agate mortar to homogenize the starting material. The typical grain size of the starting mixture was 1–5 μm, which was confirmed by using a scanning electron microscope (SEM; JEOL JSM-5410). This powdered mixture was compressed to make discs by using cylindrical jigs. The sample compositions used in this study were determined by the EPMA analysis to be $Fe_{80.1}S_{12.7}Si_{7.2}$ (Fe-8wt.%S-4wt.%Si) and $Fe_{74.4}S_{18.5}Si_{7.1}$ (Fe-12wt.%S-4wt.%Si). These compositions might be close to the composition of Mercury's core, which might contain several wt.% silicon in addition to sulfur, as was

suggested by previous high-pressure experiments under reducing conditions (e.g., Malavergne et al. 2010). The two starting materials were used for determination of the subsolidus phases and the solidus temperature of the Fe–S–Si system, whereas the liquidus temperature was determined for the starting material with $Fe_{80.1}S_{12.7}Si_{7.2}$ in composition.

We made a thin foil of starting materials by using a cold compression technique. Before loading the sample, we checked the homogeneity of the sample with a grain size less than 2 μm again by using a high-resolution reflection microscope and selected only homogeneous pieces of the mixture foil. For the in situ experiments, the sample foil was sandwiched between NaCl pellets, which worked as a pressure medium, thermal insulator, and pressure marker. These samples were loaded into a sample hole in a pre-compressed SUS304 or Re gasket, which was typically about 30–50 μm in thickness. On the other hand, the sample foil was embedded into an Al_2O_3 powder, which worked as a pressure medium, for the sample recovered experiments. When NaCl was used as a pressure medium, it was difficult to recover the sample because it flowed in the NaCl pressure medium towards the gasket during decompression.

The sample was heated by using the double-sided laser heating method (Shen et al. 1996) employing an Nd:YAG laser or fiber laser. Radiation from the heated sample was collected for time durations between 0.5 and 3 s for analyzing the temperature. The temperature measurements were performed for several tens of seconds during heating. The experimental temperature was determined as an average of the measured temperature over several tens of seconds. The temperature fluctuation during the experiments was approximately 50–100 K. The experimental pressure was determined based on the lattice parameters of NaCl using the equation of states (EOS) of the B1 phase (Brown 1999) and the B2 phase (Fei et al. 2007) of NaCl. The experimental pressure at high temperature was assumed to be $P_{HT} = P_{300\ K} + \Delta P_{th}$. $P_{300\ K}$ is a pressure at room temperature based on the third-order Birch–Murnaghan equation of state, and ΔP_{th} is a thermal pressure based on the Mie–Grüneisen relation: $P_{th} = \gamma/V[E(T, \theta_D) - E(T_0, \theta_D)]$ where $\gamma = \gamma_0(V/V_0)^q$ and $\theta_D = \theta_0(V/V_0)^{-\gamma}$. The parameters of the EOS of NaCl are summarized in Brown (1999) and Fei et al. (2007). Since NaCl has a temperature gradient from the ambient temperature to the sample temperature, the procedure by Campbell et al. (2007, 2009) was used to evaluate the thermal pressure. The EOS of iron was not used to calculate experimental pressure in this study because incorporation of silicon or sulfur into solid iron may expand the unit cell volume of iron (e.g., Hirao et al. 2004). The error in pressure was evaluated from the error in the volume of NaCl, and the error in temperature was

Sakairi *et al. Progress in Earth and Planetary Science* (2017) 4:10

Page 3 of 11

determined based on the standard deviation of the fluctuation of the measured temperature.

In situ X-ray diffraction experiments were conducted at the BL10XU beamline of the SPring-8 facility (Ohishi et al. 2008). We used a monochromatic X-ray beam with a typical wavelength of 0.4136(3) Å collimated to a diameter of 15 μm. The beam size was smaller than the size of the laser heating area, which was approximately 30–40 μm across. We checked the X-ray position by the X-ray fluorescence of diamonds before heating. Therefore, the X-ray and heating areas are aligned well. The melting detection in this study was based on the disappearance of the X-ray diffraction peaks which were the same as those in previous melting studies (e.g., Kamada et al. 2010, 2012; Terasaki et al. 2011). An imaging plate (IP: Rigaku R-AXIS IV^{++}) or an X-ray charge-coupled device (CCD: Brucker AXS, SMART APEX) was used as X-ray detectors. The typical exposure time for taking diffraction patterns was 1 s for the CCD detector or 3 min for the IP detector for each run. At high temperatures, the sample diffraction patterns were collected by using the CCD detector because it is important to take a diffraction pattern within a short duration of time to detect melting of the sample. First, the sample was compressed to a target pressure at room temperature and then annealed at around 1500 K for about 10 min to synthesize solid phases and to reduce stress in the cell assemblages. The diffraction patterns of the sample were recorded at room temperature and in the temperature ranges between 1350 and 2270 K in 50–100 K steps at each pressure. The temperature fluctuations were almost the same as those at subsolidus conditions and after melting conditions. After we observed the disappearance of the X-ray diffraction peaks of Fe$_3$S, the laser power was shut down to quench the sample. The reappearance of X-ray diffraction peaks of Fe$_3$S in the quenched sample was confirmed to be reproducible and suggests the disappearance of Fe$_3$S peaks at high temperatures was caused by the sample melting and was not caused by migration of Fe$_3$S from the heating spot of the sample. The diffraction patterns were analyzed by the IPAnalyzer software package and the PDIndexer software package programmed by Seto et al. (2010).

Results and Discussion
Subsolidus phases in the Fe–S–Si system
The experimental conditions and the observed phases are summarized in Table 1. In situ X-ray diffraction experiments were conducted in the pressure range of 20.8 to 61 GPa and the temperature range of 300 to 2270 K. In all the explored pressure ranges, the diffraction peaks of the fcc (γ) phase, and/or the hcp (ε) phase, and Fe$_3$S were observed under the subsolidus conditions of this

study for the two starting compositions of Fe$_{80.1}$S$_{12.7}$Si$_{7.2}$ (Fe-8wt.%S-4wt.%Si) and Fe$_{74.4}$S$_{18.5}$Si$_{7.1}$ (Fe-12wt.%S-4wt.%Si) as shown in Table 1. The diffraction peaks of the fcc and hcp phases were derived from the Fe–Si alloy. Fe$_3$S, which has been reported as an intermediate phase in the Fe–FeS system (e.g., Fei et al. 2000), appeared as a result of a reaction between Fe and FeS. Other possible phases in the Fe–FeS system, such as Fe$_2$S and Fe$_3$S$_2$, were not observed in this study. In this study, because of dissolution of silicon into Fe, the boundary of fcc and hcp phases shifted towards higher pressures compared to that of pure Fe. (e.g., Anzellini et al. 2013; Ma et al. 2004). Previous studies of the Fe–FeSi system (e.g., Asanuma et al. 2008) reported that silicon expanded the stability field of the fcc phase of Fe alloy and the Fe–Si alloy had a wide stability field of coexistence of hcp and fcc phases; this is consistent with the results of this study.

Solidus and liquidus temperatures in the Fe–S–Si system
We determined both the solidus and liquidus temperatures up to 61 GPa by using the X-ray diffraction patterns of the starting sample of Fe$_{80.1}$S$_{12.7}$Si$_{7.2}$, whereas only the solidus temperature was determined for the starting sample of Fe$_{74.4}$S$_{18.5}$Si$_{7.1}$. The solidus temperatures for the two compositions were in good agreement with each other. Changes in the diffraction patterns due to melting of Fe$_3$S and Fe–Si alloys were observed as shown in Fig. 1a (A–D). The 2D images of the same diffraction patterns are shown as Additional file 1: Figure S1(a). Figure 1a (A) shows the diffraction pattern of fcc/hcp Fe–Si alloy and Fe$_3$S taken at 59.2 GPa and 1490 K. The diffraction peaks from fcc/hcp Fe–Si alloy and Fe$_3$S weakened when the sample was heated to 1830 K (Fig. 1a (B)). Both the X-ray diffraction peaks of hcp Fe–Si alloy and Fe$_3$S disappeared at 1870 K, although the peaks of fcc Fe–Si alloy still remained in the diffraction pattern (Fig. 1a (C)). After quenching, the peaks of hcp Fe–Si alloy and Fe$_3$S reappeared (Fig. 1a (D)) due to crystallization from the melt. Although we could not observe diffuse scattering peaks from the melt in most runs except those made at low pressure around 10 GPa, this observation of the peak disappearance during heating and reappearance of the peaks after quenching implies strong evidence for melting of the sample. Similarly, Fe$_3$S disappeared first from the diffraction peaks, and fcc/hcp Fe–Si phases were observed at a higher temperature in the other runs. Disappearance of the diffraction peaks of Fe$_3$S was observed at 27, 44, 54, and 60 GPa. The determination of the solidus curve was also confirmed by texture observations of the recovered sample in a separate run as shown in Fig. 2. The dendritic quench texture of the recovered sample in this figure, which shows clear evidence for melting of the run product, is consistent with

Table 1 Experimental conditions and results

Run number	P^a [GPa]	T [K]	Observed phases
Fe-8wt.%S-4wt.%Si			
FESSI09_004	58(4)	1450(50)	hcp[b], fcc[b], Fe$_3$S, NaCl(B2)
FESSI09_007	59(4)	1490(50)	hcp, fcc, Fe$_3$S, NaCl(B2)
FESSI09_008	59(5)	1580(50)	hcp, fcc, Fe$_3$S, NaCl(B2)
FESSI09_009	61(4)	1700(50)	hcp, fcc, Fe$_3$S, NaCl(B2)
FESSI09_010	60(4)	1810(50)	hcp, fcc, Fe$_3$S, NaCl(B2)
FESSI09_011	60(4)	1830(50)	hcp, fcc, Fe$_3$S, NaCl(B2)
FESSI09_012	60(4)	1870(50)	fcc, NaCl(B2)[d]
FESSI09_013	58.1(0.3)	300	hcp, fcc, Fe$_3$S, NaCl(B2)
FESSI10_015	55(2)	300	hcp, fcc, Fe$_3$S, NaCl(B2)
FESSI10_016	57(4)	1520(50)	hcp, fcc, Fe$_3$S, NaCl(B2)
FESSI10_017	57(5)	1560(50)	hcp, fcc, Fe$_3$S, NaCl(B2)
FESSI10_018	58(5)	1650(50)	hcp, fcc, Fe$_3$S, NaCl(B2)
FESSI10_019	58(5)	1675(50)	hcp, fcc, Fe$_3$S, NaCl(B2)
FESSI10_020	58(5)	1740(50)	hcp, fcc, Fe$_3$S, NaCl(B2)
FESSI10_022	57(5)	1780(50)	hcp, fcc, Fe$_3$S, NaCl(B2)
FESSI10_023	56(4)	1800(50)	hcp, fcc, Fe$_3$S, NaCl(B2)
FESSI10_024	54(4)	1810(50)	hcp, fcc, Fe$_3$S, NaCl(B2)
FESSI10_025	54(4)	1840(50)	hcp, NaCl(B2)[e]
FESSI10_026	54(4)	1880(50)	hcp, NaCl(B2)[e]
FESSI10_030	49.2(0.6)	300	hcp, fcc, Fe$_3$S, NaCl(B2)
FESSI27_012	20.9(0.3)	300	hcp, fcc, Fe$_3$S, NaCl(B1)
FESSI27_013	21(2)	1275(50)	hcp, fcc, Fe$_3$S, NaCl(B1)
FESSI27_014	21(2)	1310(50)	hcp, fcc, Fe$_3$S, NaCl(B1)
FESSI27_015	21(2)	1460(50)	hcp, fcc, Fe$_3$S, NaCl(B1)
FESSI27_020	21(2)	1520(50)	hcp, fcc, NaCl(B1)
FESSI27_021	21.1(0.3)	300	hcp, fcc, Fe$_3$S, NaCl(B1)
FESSI27_028	21(2)	1760(50)	hcp, fcc, NaCl(B1)
FESSI27_029	21(2)	1950(50)	NaCl(B1)
FESSI27_030	20.8(0.3)	300	hcp, fcc, Fe$_3$S, NaCl(B1)
FESSI36_002	30.8(0.3)	300	hcp, fcc, Fe$_3$S, NaCl(B2)
FESSI36_003	33(4)	1430(50)	hcp, fcc, Fe$_3$S, NaCl(B2)
FESSI36_004	32(3)	1500(50)	hcp, fcc, Fe$_3$S, NaCl(B2)
FESSI36_005	33(4)	1550(50)[c]	hcp, fcc, Fe$_3$S, NaCl(B2)
FESSI36_006	33(4)	1660(50)[c]	hcp, fcc, Fe$_3$S, NaCl(B2)
FESSI36_007	35(4)	1790(50)	hcp, fcc, NaCl(B2)
FESSI36_008	33(4)	1840(50)	hcp, fcc, NaCl(B2)
FESSI36_009	32(5)	1910(50)[c]	fcc, NaCl(B2)
FESSI36_010	34(5)	2010(50)[c]	NaCl(B2)
FESSI36_011	34(4)	2030(80)	NaCl(B2)
FESSI36_012	30.7(0.3)	300	hcp, fcc, Fe$_3$S, NaCl(B2)
FESSI36_026	51.1(0.8)	300	hcp, fcc, Fe$_3$S, NaCl(B2)
FESSI36_027	50(4)	1620(50)	hcp, fcc, Fe$_3$S, NaCl(B2)

Table 1 Experimental conditions and results (Continued)

FESSI36_028	50(4)	1865(50)[c]	hcp, fcc, Fe_3S, NaCl(B2)
FESSI36_029	49(5)	2150(50)[c]	hcp, fcc, NaCl(B2)
FESSI36_030	51(5)	2270(60)	NaCl(B2)
FESSI36_031	47.5(0.2)	300	hcp, fcc, Fe_3S, NaCl(B2)
FESSI36_032	55.0(0.5)	300	hcp, fcc, Fe_3S, NaCl(B2)
Fe-12wt.%S-4wt.%Si			
FESSI19_005	24.9(0.1)	300	hcp, fcc, Fe_3S,NaCl(B1,B2)
FESSI19_006	26(3)	1350(50)	hcp, fcc, Fe_3S,NaCl(B1,B2)
FESSI19_007	27(3)	1410(50)	hcp, fcc, Fe_3S,NaCl(B1,B2)
FESSI19_008	26(3)	1390(50)	hcp, fcc, Fe_3S,NaCl(B1,B2)
FESSI19_009	27(3)	1470(50)	hcp, fcc, Fe_3S,NaCl(B1,B2)
FESSI19_013	27(3)	1460(50)	hcp, fcc, Fe_3S,NaCl(B1,B2)
FESSI19_014	27(3)	1610(75)	hcp, NaCl(B1,B2)[e]
FESSI19_016	24.4(0.1)	300	hcp, fcc, Fe_3S,NaCl(B1,B2)
FESSI20_002	42.1(0.4)	300	hcp, Fe_3S, NaCl(B2)
FESSI20_003	44(3)	1345(50)	hcp, Fe_3S, NaCl(B2)
FESSI20_004	44(3)	1450(50)	hcp, Fe_3S, NaCl(B2)
FESSI20_005	44(3)	1480(50)	hcp, Fe_3S, NaCl(B2)
FESSI20_006	44(3)	1500(50)	hcp, Fe_3S, NaCl(B2)
FESSI20_007	44(3)	1570(50)	hcp, Fe_3S, NaCl(B2)
FESSI20_008	44(4)	1650(50)	hcp, Fe_3S, NaCl(B2)
FESSI20_013	44(4)	1730(50)	hcp, NaCl(B2)[e]
FESSI20_015	42.2(3)	300	hcp, fcc, Fe_3S, NaCl(B2)

The numbers in parentheses show errors
The melting of the sample was detected by disappearance of diffraction pattern
[a]The pressures are based on the EOS of NaCl(B1) (Brown, 1999) and NaCl(B2) (Fei et al., 2007)
[b]hcp and fcc represent the structure of Fe–Si alloy
[c]The temperatures are estimated by the laser power
[d]hcp-Fe–Si is expected to exist, although it is not observed
[e]fcc-Fe–Si is expected to exist, although it is not observed in the X-ray diffraction
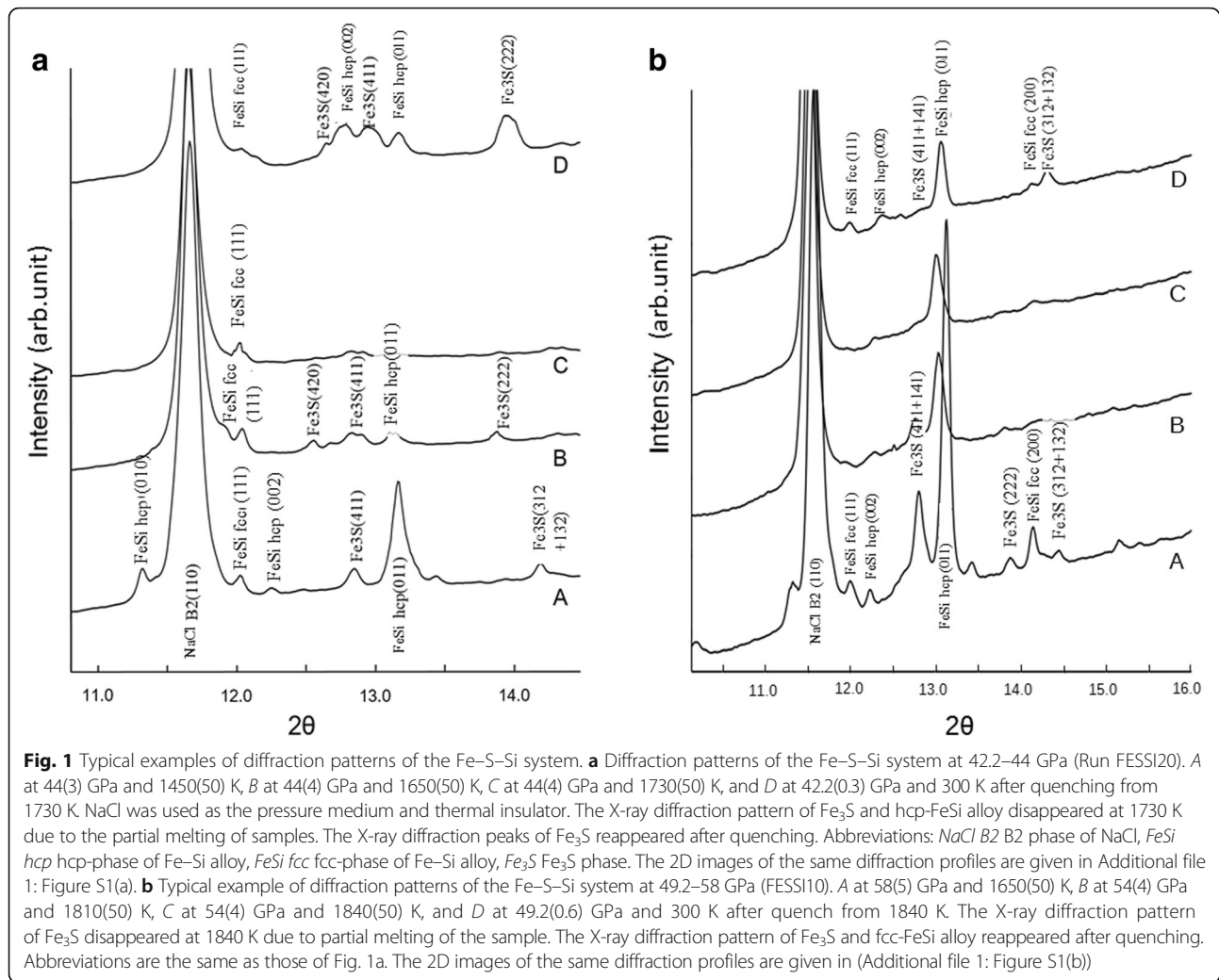
the melting curve determined by in situ X-ray diffraction experiments. Figure 1b (A–D) shows similar change in diffraction profiles obtained in the pressure range of 49.2–58 GPa. The diffraction peaks of fcc/hcp Fe–Si alloy and Fe_3S were observed under subsolidus conditions at 58 GPa and 1650 K. The X-ray diffraction peaks of Fe_3S weakened with increasing temperature to 1810 K (B) and disappeared at 1840 K and 54 GPa (C). After quenching, the peaks of fcc/hcp Fe–Si alloy and Fe_3S reappeared (D). The 2D images of the same diffraction profiles are given in the (Additional file 1: Figure S1(b)).

We observed the disappearance of the diffraction peaks from fcc/hcp Fe–Si alloy and Fe_3S. This disappearance suggests that total melting occurred in the Fe–S–Si system at 21, 34, 51 and 58 GPa for the bulk composition of $Fe_{80.1}S_{12.7}Si_{7.2}$ (Table 1).

Melting of Fe_3S corresponds to the solidus temperature, and the complete disappearance of both fcc/hcp Fe–Si alloy and Fe_3S corresponds to the liquidus temperature of

the Fe–S–Si system. Based on these melting sequences, the phase relations of the Fe–S–Si system are drawn in Fig. 3. Both the solidus and liquidus temperatures increase with increasing pressure. This criterion for determination of melting was also used by Terasaki et al. (2011), and melting was also confirmed by the observation of the quench textures of dendrite in the recovered samples after quenching at high pressure and temperature. The compositional change in the Fe–S–Si system with pressure and temperature is very important. However, the measurement of the compositions of the phases was very limited in this work due to technical difficulties. We used NaCl as the pressure medium and pressure marker; however, the samples in the NaCl pressure medium were difficult to recover due to its large deformation during decompression and recovery. We conducted recovery experiments using alumina pressure medium. We analyzed the composition of coexisting crystalline phases in a run conducted at 58(4) GPa and 1940(110) K. The

Sakairi *et al. Progress in Earth and Planetary Science* (2017) 4:10

Page 6 of 11

Fig. 1 Typical examples of diffraction patterns of the Fe–S–Si system. **a** Diffraction patterns of the Fe–S–Si system at 42.2–44 GPa (Run FESSI20). *A* at 44(3) GPa and 1450(50) K, *B* at 44(4) GPa and 1650(50) K, *C* at 44(4) GPa and 1730(50) K, and *D* at 42.2(0.3) GPa and 300 K after quenching from 1730 K. NaCl was used as the pressure medium and thermal insulator. The X-ray diffraction pattern of Fe3S and hcp-FeSi alloy disappeared at 1730 K due to the partial melting of samples. The X-ray diffraction peaks of Fe3S reappeared after quenching. Abbreviations: *NaCl B2* B2 phase of NaCl, *FeSi hcp* hcp-phase of Fe–Si alloy, *FeSi fcc* fcc-phase of Fe–Si alloy, *Fe3S* Fe3S phase. The 2D images of the same diffraction profiles are given in Additional file 1: Figure S1(a). **b** Typical example of diffraction patterns of the Fe–S–Si system at 49.2–58 GPa (FESSI10). *A* at 58(5) GPa and 1650(50) K, *B* at 54(4) GPa and 1810(50) K, *C* at 54(4) GPa and 1840(50) K, and *D* at 49.2(0.6) GPa and 300 K after quench from 1840 K. The X-ray diffraction pattern of Fe3S disappeared at 1840 K due to partial melting of the sample. The X-ray diffraction pattern of Fe3S and fcc-FeSi alloy reappeared after quenching. Abbreviations are the same as those of Fig. 1a. The 2D images of the same diffraction profiles are given in (Additional file 1: Figure S1(b))

analyses revealed that the Si content was approximately 12.4 at.% in the metallic Fe–Si phase in the periphery of the laser spot of the recovered sample from 58(4) GPa and 1940(110) K conditions, whereas it was only 0.4 at.% in the Fe3S phase adjacent to the Fe-Si alloy. Further work is needed for determination of the compositional variation among coexisting phases in this system with pressure and temperature.

The solidus and liquidus curves were fitted by the Simon equation (Simon and Glatzel 1929), $Tm = T_m^R \times \left(\frac{P - P^R}{a} + 1 \right)^{\frac{1}{c}}$, as adopted by previous studies (e.g., Asanuma et al. 2010; Terasaki et al. 2011), where T_m is the melting temperature in Kelvins at an experimental pressure (P) in GPa, T_m^R is the melting temperature at a reference pressure, and P^R, a, and c are fitting parameters. The parameters fitted are T_m^R = 1432(6), a = 122(2), and c = 1.10(2) for the solidus and T_m^R = 1768(13), a = 145(5), and c

= 0.99(3) for the liquidus assuming the reference pressure of P^R = 15 GPa. When we assume the reference pressure of P^R = 0 GPa, the parameters fitted are T_m^R = 1277(6), a = 116.1(2.1), and c = 1.06(0.02) for the solidus and T_m^R = 1582(13), a = 127.9(4.8), and c = 1.00(0.03) for the liquidus. The solidus and liquidus curves with different reference pressures are nearly the same, and the reference pressures do not affect the following discussions.

Sulfur and silicon are candidates for the light elements in the cores of Earth, Mars, and Mercury (e.g., Malavergne et al. 2007; Sanloup and Fei 2004). Thus, the present results on the solidus and liquidus temperatures can be applicable to the core formation processes in the terrestrial planets. Figure 4 summarizes the liquidus and solidus temperatures of iron-light element systems (Campbell et al. 2007; Chudinovskikh and Boehler 2007; Morard et al. 2008; Asanuma et al. 2010; Terasaki et al. 2011; Kamada et al. 2012) and peridotite (Fiquet et al. 2010; Zhang and Herzberg 1994).
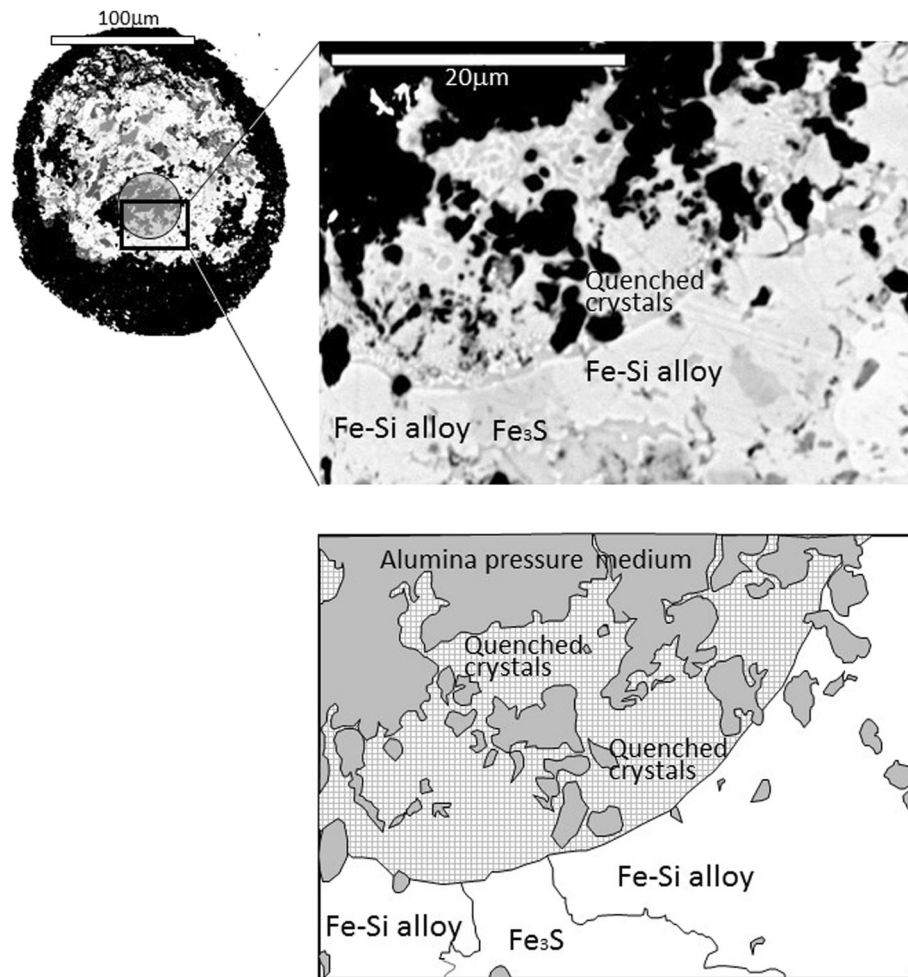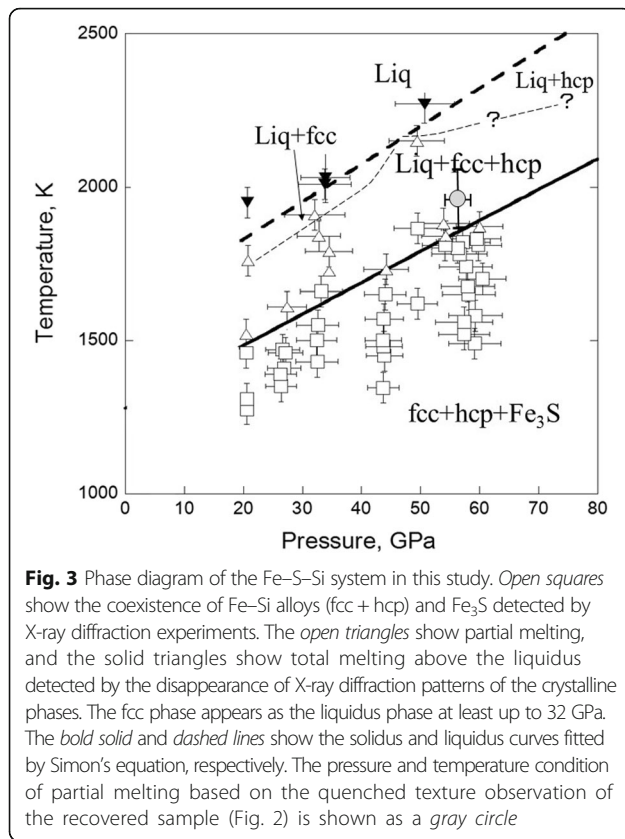
Fig. 2 Back scattered electron (BSE) image of the quench textures of the melting experiment. The sample was recovered from 58(4) GPa and 1940(110). The experimental conditions are shown as a *gray circle* in the phase diagram given in Fig. 3. A zoom-out image of the sample in DAC is shown in this figure. The diameter of the laser beam is around 40 μm and is shown as a *gray circle* in the figure. The detailed textures of the zoom-in image are also *sketched at the bottom* of the BSE image. A dendritic texture showing quenching from the melt is clearly observed in the BSE image and shown as *hatched areas* in the sketch. The *black grains* in the zoom-in and zoom-out images are alumina grains used for the pressure medium. It was difficult to remove the alumina grains from the sample during surface polishing

The liquidus temperature in this study is about 500 K lower than that of pure Fe (Anzellini et al. 2013; Ma et al. 2004). In addition, the present liquidus curve in Fe–Si–S is lower than the melting temperature in the Fe–Si alloy reported by Asanuma et al. (2010) and close to the liquidus of the Fe–S–O system (Terasaki et al. 2011). The present solidus of the Fe–S–Si system is very close to the eutectic temperature of the Fe–S system (Campbell et al. 2007; Chudinovskikh and Boehler 2007; Morard et al. 2008: Kamada et al. 2012) and the solidus of the Fe–S–O system (Terasaki et al. 2011) within experimental uncertainties. This result indicates that the effect of the addition of Si and O on the depression of eutectic temperatures in the Fe–S system is very small.

The Fe–S–Si system has a very low solidus temperature compared to the solidus of the silicate mantle, which indicates that heating during accretion of the Earth created a metallic melt in crystalline silicates, and the core separation perhaps started by percolation of a eutectic-like metallic melt with S enrichment in the silicate mantle early in the accretion of the planetesimals (Terasaki et al. 2005). The thermal models of Mars and Mercury (Breuer et al. 2007; Solomon 1976; Toksoz et al. 1978) indicate that the internal temperatures approached the solidus temperature of the silicate mantle and the magma ocean occurred early in the histories of these planets. By assuming that the cores of the planets contain both S and Si as light elements (Malavergne et al. 2007; Malavergne et al. 2010), the models of the thermal history of these planets suggest that, during their formation, the temperature in their centers approached or exceeded the liquidus temperature

Sakairi *et al. Progress in Earth and Planetary Science* (2017) 4:10

Page 8 of 11

Fig. 3 Phase diagram of the Fe–S–Si system in this study. *Open squares* show the coexistence of Fe–Si alloys (fcc + hcp) and Fe₃S detected by X-ray diffraction experiments. The *open triangles* show partial melting, and the solid triangles show total melting above the liquidus detected by the disappearance of X-ray diffraction patterns of the crystalline phases. The fcc phase appears as the liquidus phase at least up to 32 GPa. The *bold solid* and *dashed lines* show the solidus and liquidus curves fitted by Simon's equation, respectively. The pressure and temperature condition of partial melting based on the quenched texture observation of the recovered sample (Fig. 2) is shown as a *gray circle*

Fig. 4 The melting curves of Fe and Fe-light element systems. Temperature profiles of the cores of Mars and Mercury are also shown. The *bold solid lines* are Sol and Liq, which show the solidus and liquidus temperatures of the Fe₈₀.₁S₁₂.₇Si₇.₂ composition in the Fe–S–Si system. The adiabatic temperature of the core of Mercury estimated by this work, 27 K/GPa, is given as a *red curve*, S, under the assumption that the temperature at CMB of Mercury is 1800 K (e.g., Dumberry and Rivoldini 2015; Malavergne et al. 2010). The temperature profiles of the Martian core estimated by Fei and Bertka (2005), and Mercury's core by Dumberry and Rivoldini (2015) are also shown as FB and DR, respectively. The previously reported melting curves of Fe-light element systems and solidus of peridotite are shown in this figure as follows. Melting curve of Fe by Anzellini et al. (2013) is labeled as *FeA*; melting curve of Fe–Si by Asanuma et al. (2010) is labeled as *Fe–SiA*; solidus of the Fe–S system reported by Kamada et al. (2012) is labeled as *Fe–S K*; liquidus of Fe–S by Chen et al. (2008) is labeled as *Fe–S C*; solidus and liquidus temperatures for a composition of Fe₇₅O₅S₂₀ reported by Terasaki et al. (2011) are labeled as *Fe-O-S(S)* and *Fe-O-S(L)*, respectively. Also the eutectic of the Fe–S system by Campbell et al. (2007) is *Fe–S CP*; the eutectic of Fe–S by Morard et al. (2008) is *Fe–S M*; the eutectic of Fe-FeS by Chudinovskikh and Borhler (2007) is *Fe–S CB*; the solidus temperature of peridotite by Fiquet et al. (2010) is labeled as *Peridotite F* and that by Zhang and Herzberg (1994) is labeled as *Peridotite ZH*. The pressure conditions for the cores of Mercury and Mars are shown as shaded areas, *yellow* and *gray*, respectively

of the Fe–Si–S system after the magma ocean stage. Thus, the cores of these planets were once molten in the early stage of their core formation.

Existence of an ancient magnetic field in Mercury (Johnson et al. 2015) implies the operation of a dynamo in the molten core in Mercury's early history. Recent works on longitude libration of Mercury showed that the mantle and core of Mercury are decoupled, and thus, Mercury's core is at least partially molten (e.g., Margot et al. 2007; Riner et al. 2008).

Assuming that the core of Mercury is composed of iron alloy with minor amounts of sulfur and silicon and more likely to be under the reducing core conditions of the planet, we can estimate the adiabatic gradient of the molten core of the planet. The adiabatic gradient of the molten core can be expressed as follows (Anderson 1998):

$$\left(\frac{\partial \ln T}{\partial \ln \rho}\right)_s = \gamma_{\text{th}}$$

where T is a temperature at a certain depth in the outer core, ρ is the density of the core at that depth, and γ_{th} is the thermodynamic Grüneisen parameter. Therefore, the
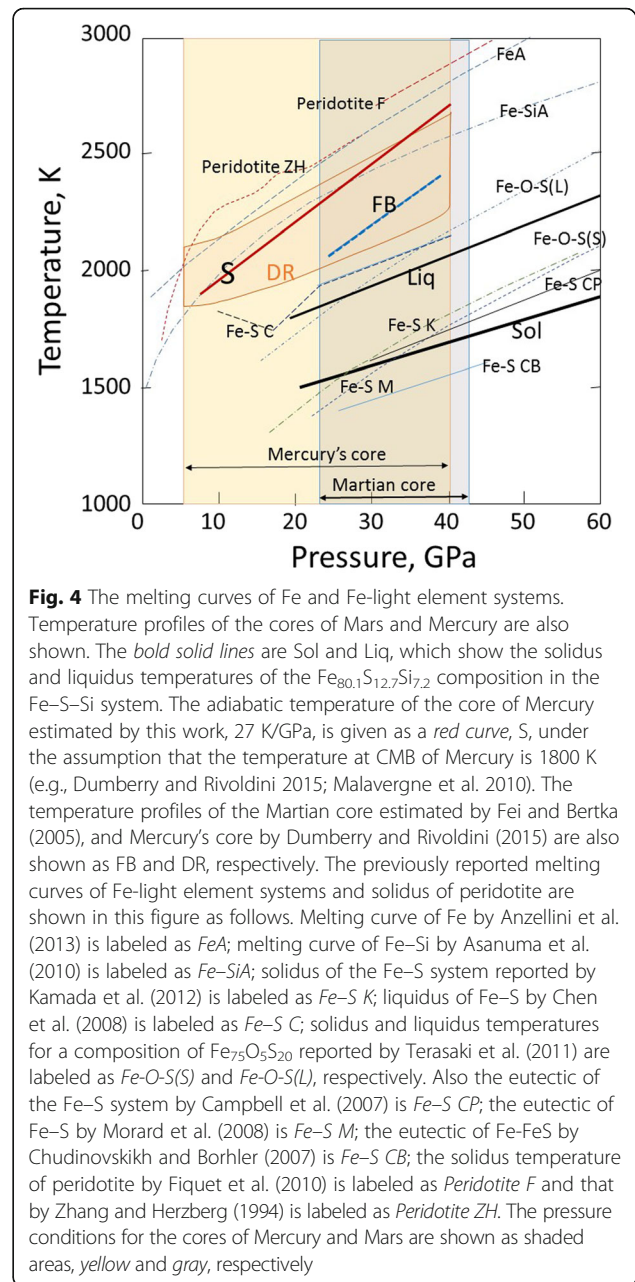
core–mantle boundary (CMB) temperature can be calculated as follows:

$$T_{\text{CMB}} = T_{\text{ICB}} \left(\frac{\rho_{\text{CMB}}}{\rho_{\text{ICB}}}\right)^{\gamma_{\text{th}}}$$

where T_{CMB} and T_{ICB} are temperatures at the CMB and the ICB conditions, respectively, and ρ_{CMB} and ρ_{ICB} are densities of the molten core at CMB and ICB, respectively. To calculate the adiabatic temperature gradients under the liquid core conditions, the thermodynamic

Sakairi *et al. Progress in Earth and Planetary Science* (2017) 4:10

Page 9 of 11

Grüneisen parameter γ_{th} of the outer core may be around 1.3 (Anderson 1998; Dubrovinsky 2000; Stacey 1995; Vocadlo et al. 2000). However, it could have a large uncertainty. Therefore, we assumed γ_{th} to be in the range of 1.0–1.5. The density of molten metal in the core of Mercury may be taken to be the density of the Fe–S melt (Sanloup et al. 2000, 2002; Terasaki 2015) or the Fe–Si melt at high pressure (Tateyama et al. 2011; Yu and Secco 2008; Nishida et al. 2011; Terasaki 2015), and the CMB temperatures are assumed to be around 1770 K for Mercury and 1990 K for Mars (e.g., Dumberry and Rivoldini 2015; Malavergne et al. 2010). Based on these parameters with the above thermodynamic relations, the adiabatic temperature gradients of the liquid cores were calculated to be around 27(6) K/GPa for Mercury and 18(4) K/GPa for Mars. The adiabatic temperature gradient is consistent with that estimated by Fei and Bertka (2005) for the Martian core, and it is consistent but slightly greater than that estimated by Dumberry and Rivoldini (2015) for Mercury's core as shown in Fig. 4.

The slope of the liquidus temperature of the Fe–S–Si system, approximately 12 K/GPa, is half of the adiabatic temperature gradient of the Mercury and Martian cores. Although the liquidus temperature can be changed with the bulk composition of the metal systems and thus the slope of the liquidus curve could change with the composition, the above conclusion is valid for the liquidus temperatures for various bulk compositions of the Fe–Si–S system since the slopes of the liquidus temperatures of the end member systems of Fe–S and Fe–Si are significantly smaller than the adiabatic gradient of the planets (e.g., Chen et al. 2008; Asanuma et al. 2010). Therefore, crystallization of the core of the planets must have started at CMB. This crystallization start is consistent with the snowing-core model proposed for Ganymede (Hauck et al. 2006) and Mars (Stewart et al. 2007).

The liquidus curve determined here for the present composition of the Fe–S–Si system relevant to Mercury's core is slightly lower than that of the Fe–S system with the same S content estimated by Chen et al. (2008), i.e., the existence of Si slightly lowers the liquidus of the Fe–S system. The conclusion of snowing in Mercury's core with the assumption of the Fe–S core suggested by Chen et al. (2008) is also valid for the Si and S bearing core model of Mercury, which is more likely under the reducing conditions in Mercury's core. The crystals falling into the core could be dissolved again in the molten core, which would make it difficult to maintain the layered core structure composed of a completely molten outer core and a crystalline inner core in the planets. However, when the core adiabat is located between the solidus and liquidus temperatures of the core materials during cooling, we can expect core stratification in the form of a partially crystallizing outer core and precipitated crystalline inner core.

Conclusions

The phase and melting relations in the Fe–S–Si system were studied up to 60 GPa by using a double-sided laser-heated diamond anvil cell combined with X-ray diffraction. We confirmed that hcp/fcc Fe–Si alloys and Fe_3S are stable phases under subsolidus conditions in the system. The liquidus phase changes from fcc to hcp at around 40 GPa. Both solidus and liquidus temperatures are significantly lower than the melting temperature of pure Fe and both increase with increasing pressure. The slope of the Fe–S–Si liquidus temperature determined here is 12 K/GPa, which is significantly smaller than the adiabatic temperature gradients of the liquid cores of Mercury and Mars, at around 18~27 K/GPa. Thus, crystallization of their cores started at the core–mantle boundary region even in the cores containing both silicon and sulfur as light elements. This crystallization start is consistent with the snowing-core model proposed by previous authors for the cores with the Fe–S systems (Chen et al. 2008; Stewart et al. 2007).

Additional file

Additional file 1: a 2D images of diffraction patterns of the Fe–S–Si system at 42.3–44.1 GPa (Run FESSI20) corresponding to the X-ray profile given in Figure 1(a). A at 44(1) GPa and 1450(50) K, B at 44(4) GPa and 1650(50) K, C at 44(4) GPa and 1730(50) K, and D at 42.2(0.3) GPa and 300 K after quenching from 1730 K. NaCl was used as the pressure medium and thermal insulator. b 2D images of diffraction patterns of the Fe–S–Si system at 49.2-58.2 GPa (Run FESSI10) corresponding to the X-ray profile given in Figure 1(b). A at 58(5) GPa and 1650(50) K, B at 54(4) GPa and 1810(50) K, C at 54(4) GPa and 1840(50) K, and D at 49.2(0.6) GPa and 300 K after quenching from 1840 K. (DOCX 1725 kb)

Abbreviations

BSE: Back-scattered electron image; CCD: Charge-coupled device; CMB: Core–mantle boundary; DAC: Diamond anvil cell; EOS: Equation of state; EPMA: Electron probe micro-analyzer; ICB: Inner core boundary; LHDAC: Laser-heated diamond anvil cell; SEM: Scanning electron microscope; YAG: Yttrium aluminium garnet

Sakairi *et al. Progress in Earth and Planetary Science* (2017) 4:10

Page 10 of 11

Author details
[1]Department of Earth and Planetary Materials Science, Graduate School of Science, Tohoku University, Sendai 980-8578, Japan. [2]V.S. Sobolev Institute of Geology and Mineralogy, Siberian Branch, Russian Academy of Sciences, Koptyuga Ave. 3, Novosibirsk 630090, Russia. [3]Frontier Research Institute for Interdisciplinary Science, Tohoku University, Sendai 980-8578, Japan. [4]Geodynamics Research Center, Ehime University, Matsuyama 790-8577, Japan. [5]Japan Synchrotron Radiation Research Institute, Hyogo 679-5198, Japan.

References
Allégre CJ, Poirier JP, Humler E, Hofmann AW (1995) The chemical composition of the Earth. Earth Planet Sci Lett 134:515–526

Anderson OL (1998) The Grüneisen parameter for iron at outer core conditions and the resulting conductive heat and power in the core. Phys Earth Planet Inter 109:179–197

Anzellini S, Dewaele A, Mezouar M, Loubeyre P, Morard G (2013) Melting of iron at Earth's inner core boundary based on fast X-ray diffraction. Science 340:464–466

Asanuma H, Ohtani E, Sakai T, Terasaki H, Kamada S, Hirao N, Sata N, Ohishi Y (2008) Phase relations of Fe-Si alloy up to core conditions: implications for the Earth inner core. Geophys Res Lett 35, L12307

Asanuma H, Ohtani E, Sakai T, Kamada S, Terasaki H, Kondo T, Kikegawa T (2010) Melting of iron-silicon alloy up to the core–mantle boundary pressure: implications to the thermal structure of the Earth's core. Phys Chem Minerals 37:353–359

Bertka CM, Fei Y (1998) Density profile of an SNC model Martian interior and the moment-of-inertia factor of Mars. Earth Planet Sci Lett 157:79–88

Birch F (1964) Density and composition of mantle and core. J Geophys Res 69:4377–4388

Boehler R (1996) Melting and element partitioning Fe-FeS eutectic temperatures to 620 kbar. Phys Earth Planet Inter 96:181–186

Breuer D, Hauck IISA, Buske M, Pauer M, Spohn T (2007) Interior evolution of Mercury. Space Sci Rev 132:229–260

Brown JM (1999) The NaCl pressure standard. J Appl Phys 86:5801–5808

Campbell AJ, Seagle CT, Heinz D, Shen G, Prakapenka VB (2007) Partial melting in the iron-sulfur system at high pressure: a synchrotron X-ray diffraction study. Phys Earth Planet Inter 162:119–128

Chen B, Li J, Hauck SAII (2008) Non-ideal liquidus curve in the Fe-S system and Mercury's snowing core. Geophys Res Lett 35:L07201

Chudinovskikh L, Boehler R (2007) Eutectic melting in the Fe-S system to 44 GPa. Earth Planet Sc Lett 257:97–103

Dubrovinsky LS, Saxena SK, Dubrovinskaia NA, Rekhi S, Le Bihan T (2000) Grüneisen parameter of e-iron up to 300 GPa from in-situ X-ray study. Am Mineral 85:386–389

Dumberry M, Rivoldini A (2015) Mercury's inner core size and core-crystallization regime. Icarus 248:254–268

Fei Y, Bertka CM (2005) The interior of Mars. Science 308:1120–1121

Fei Y, Bertka CM, Finger LW (1997) High-pressure iron-sulfur compound, Fe_3S_2, and melting relations in the Fe-FeS system. Science 275:1621–1623

Fei Y, Li J, Bertka CM, Prewitt CT (2000) Structure type and bulk modulus of Fe_3S, a new iron-sulfur compound. Am Mineral 85:1830–1833

Fei Y, Ricolleau A, Prank M, Mibe K, Shen G, Prkapenka V (2007) Toward an internally consistent pressure scale. Proc Natl Acad Sci 104:9182–9186

Fiquet G, Auzende AL, Siebert J, Corgne A, Bureau H, Ozawa H, Garbarino G (2010) Melting of peridotite to 140 gigapascals. Science 329:1516–1518

Fischer RA, Campbell AJ, Reaman DM, Miller NA, Heinz DL, Dera P, Prakapenka VB (2013) Phase relations in the Fe-FeSi system at high pressures and temperatures. Earth Planet Sci Lett 373:54–64

Hauck SA, Aurnau JM, Dombard MJ (2006) Sulfur's impact on core evolution and magnetic field generation on Ganymede. J Geophys Res 111:E09008

Hillgren V, Gessman CK, Li J (2000) An experimental perspective on the light element in Earth's core. In: Canup RM, Righter K (eds) Origin of the Earth and Moon. The University of Arizona, Tuscon, pp 245–263

Hirao N, Ohtani E, Kondo T, Kikegawa T (2004) Equation of state of iron-silicon alloys to megabar pressure. Phys Chem Min 31:329–336

Javoy M (1995) The integral enstatite chondrite model of the Earth. Geophys Res Lett 22:2219–2222

Johnson CL, Phillips RJ, Purucker ME, Anderson BJ, Byrne PK, Denevi BW, Feinberg JM, Hauck SA II, Head JW III, Korth H, James PB, Mazarico E, Neumann GA, Philpott LC, Siegler MA, Tsyganenko NA, Solomon SC (2015) Low-altitude magnetic field measurements by MESSENGER reveal Mercury's ancient crustal field. Science. doi:10.1126/science.aaa8720

Kamada S, Terasaki H, Ohtani E, Sakai T, Kikegawa T, Ohishi Y, Hirao N, Sata N, Kondo T (2010) Phase relationships of the Fe-FeS system in conditions up to the Earth's outer core. Earth Planet Sci Lett 294:94–100

Kamada S, Ohtani E, Terasaki H, Sakai T, Miyahara M, Ohishi Y, Hirao N (2012) Melting relationships in the $Fe-Fe_3S$ system up to the outer core conditions. Earth Planet Sci Lett 359–360:26–33

Kuwayama Y, Hirose K (2004) Phase relations in the system Fe-FeSi at 21 GPa. Am Mineral 89:273–276

Li J, Fei Y, Mao HK, Hirose K, Shieh SR (2001) Sulfur in the Earth's inner core. Earth Planet Sci Lett 193:509–514

Lin JF, Heinz DL, Campbell AJ, Devine JM, Shen G (2002) Iron-silicon alloy in Earth's core? Science 295:313–315

Ma Y, Somayazulu M, Shen G, Mao HK, Shub J, Hemley RJ (2004) In situ X-ray diffraction studies of iron to Earth-core conditions. Phys Earth Planet Inter 85:319–337

Malavergne V, Tarrida M, Combes R, Bureau H, Jones J, Schwandt C (2007) New high-pressure and high-temperature metal/silicate partitioning of U and Pb: implications for the cores of the Earth and Mars. Geochim Cosmochim Acta 71:2635–2655

Malavergne V, Toplis MJ, Berthet S, Jones J (2010) Highly reducing conditions during core formation on Mercury: implications for internal structure and the origin of a magnetic field. Icarus 206:199–209

Margot J-L, Peale SJ, Jurgens RF, Slade MA, Holin IV (2007) Large longitude libration of Mercury reveals a molten core. Science 316:710–714

McDonough WF (2014) Compositional model for the Earth's core. In: Carlson RW (ed) The mantle and core. Elsevier, Amsterdam, pp 559–577

Morard G, Katsura T (2010) Pressure-temperature cartography of Fe-S-Si immiscible system. Geochim Cosmochim Acta 74:3659–3667

Morard G, Andrault D, Guignot N, Sanloup C, Mezouar M, Petitgirard S, Fiquet G (2008) In-situ determination of $Fe-Fe_3S$ phase diagram and liquid structural properties up to 65 GPa. Earth Planet Sci Lett 272:620–626

Nishida K, Ohtani E, Urakawa S, Suzuki A, Sakamaki T, Terasaki H, Katayama Y (2011) Density measurement of liquid FeS at high pressures using synchrotron X-ray absorption. Am Mineral 96:864–868

Ohishi Y, Hirao N, Sata N, Hirose K, Takata M (2008) Highly intense monochromatic X-ray diffraction facility for high-pressure research at SPring-8. High Pressure Res 28:163–173

Ozawa H, Hirose K, Suzuki T, Ohishi Y, Hirao N (2013) Decomposition of Fe3S above 250 GPa. Geophys Res Lett 40:4845–4848

Poirier JP (1994) Light elements in the Earth's outer core: a critical review. Phys Earth Planet Inter 6:123–130

Riner MA, Bina CR, Robinson MS, Desch SJ (2008) Internal structure of Mercury: implications of a molten core. Jour Geophys Res 113, E08013. doi:10.1029/2007JE002993

Sakai T, Kondo T, Ohtani E, Terasaki H, Endo N, Kuba T, Suzuki T, Kikegawa T (2006) Interaction between iron and post-perovskite at core-mantle boundary and core signature in plume source region. Geophys Res Lett 33, L15317

Sanloup C, Fei Y (2004) Closure of the Fe-S-Si liquid miscibility gap at high pressure. Phys Earth Planet Inter 147:57

Sanloup C, Guyot F, Gillet P, Fiquet G, Mezouar M, Martinez I (2000) Density measurements of liquid Fe-S alloys at high-pressure. Geophysical Res Lett 27:811–814

Sakairi *et al. Progress in Earth and Planetary Science* (2017) 4:10

Page 11 of 11

Sanloup C, Guyot F, Gillet P, Fei Y (2002) Physical properties of liquid Fe alloys at high pressure and their bearings on the nature of metallic planetary cores. J Geophys Res 107:2272. doi:10.1029/2001JB000808

Seto Y, Nishio-Hamane D, Nagai T, Sata N (2010) Development of a software suite on X-ray diffraction experiments. Rev High Pressure Sci Technol 20:269–276

Shen G, Mao HK, Hemley RJ (1996) Laser-heated diamond anvil cell technique: double-sided heating with multimode Nd:YAG laser. Advanced Materials'96– New Trends in High Pressure Research. Nat. Inst. Res. Inorg. Mater, Tsukuba, pp 149–152

Simon FE, Glatzel GC (1929) Remarks on fusion pressure curve. Z Anorg Allg Chem 178:309

Solomon SC (1976) Some aspects of core formation in Mercury. Icarus 28:509–521

Stacey FD (1995) Theory of thermal and elastic properties of the lower mantle and core. Phys Earth Planet Inter 89:219–245

Stewart AJ, Schmidt MW, Westrenen WV, Liebske C (2007) Mars: a new core-crystallization regime. Science 316:1323–1325

Tateno S, Kuwayama Y, Hirose K, Ohishi Y (2015) The structure of Fe–Si alloy in Earth's inner core. Earth Planet Sci Lett 418:11–19

Tateyama R, Ohtani E, Terasaki H, Nishida K, Shibazaki Y, Suzuki A, Kikegawa T (2011) Density measurements of liquid Fe-Si alloys at high pressure using sink-float method. Phys Chem Minerals 38:801–807

Terasaki H (2015) Physical properties of the outer core. In: Terasaki, H. and Fischer, Ch. 11, Deep Earth: Physics and Chemistry of the lower mantle and core. Geophysical Monograph series, Volume 217, American Geophys. Union, pp. 129–142.

Terasaki H, Frost DJ, Rubie DC, Langenhorst F (2005) The effect of oxygen and sulphur on the dihedral angle between Fe-O-S melt and silicate minerals at high pressure: implications for Martian core formation. Earth Planet Sci Lett 232:379–392

Terasaki H, Kamada S, Sakai T, Ohtani E, Hirao N, Ohishi Y (2011) Liquidus and solidus temperatures of a Fe-O-S alloy up to the pressures of the outer core: implication for the thermal structure of the Earth's core. Earth Planet Sci Lett 304:559–564

Toksoz MN, Hsui AT, Johnston DH (1978) Thermal evolutions of the terrestrial planets. Earth Moon Planets 18:281–320

Vocadlo L, Poirer JP, Price GD (2000) Grüneisen parameters and isothermal equations of state. Am Mineral 85:390–395

Yu X, Secco RA (2008) Equation of state of liquid Fe-17wt %Si to 12 GPa, High Press. Res., 28, 19–28.

Zhang J, Herzberg C (1994) Melting experiments on anhydrous peridotite KLB-1 from 5.0 to 22.5 GPa. J Geophys Res 99:17729–17742